



Localizing microwave heat by surface polarization of titanate nanostructures for enhanced catalytic reaction efficiency

Tuo Ji^a, Rui Tu^b, Licheng Li^c, Liwen Mu^a, Chang Liu^b, Xiaohua Lu^b, Jiahua Zhu^{a,*}

^a Intelligent Composites Laboratory, Department of Chemical and Biomolecular Engineering, The University of Akron, Akron, OH, 44325 USA

^b State Key Laboratory of Material-Oriented Chemical Engineering, College of Chemistry and Chemical Engineering Department, Nanjing Tech University, Nanjing, 210009, PR China

^c College of Chemical Engineering, Nanjing Forestry University, Nanjing, 210037, PR China



ARTICLE INFO

Keyword:

Microwave
Surface polarization
HMF
Saccharide
Biomass

ABSTRACT

Microwave has been traditionally used as fast and uniform heating source in chemical reactions, where polar solvent is often required to generate heat under microwave irradiation. In this work, solid acid catalysts were synthesized with engineered surface polarity and microwave absorption. Therefore, heat generation and reaction can be coupled at catalyst surface to improve the overall energy efficiency of reactions. Specifically, titanate nanostructures (nanocube, nanotube and nanobelt) were synthesized by using different alkalis in hydrothermal reactions. The titanate intermediates (protonated titanates, $H_2Ti_nO_{2n+1}$, $n = 3, 5$) have been demonstrated critical in controlling the catalyst pore structure, surface area, crystal composition and the quantity of acid sites. Especially, the open crystal structure of $H_2Ti_3O_7$ allowed interlayer polarization of titanates, which was critical to enable a large number of $Ti-O-SO_4^{2-}$ acid sites. The $Ti-O-SO_4^{2-}$ not only serves as catalytic active site, but also offers heat generation capability under microwave irradiation. Among the titanate nanostructures, titanate nanotube shows the best heat generation capability and gives the largest rate constant of 0.31 min^{-1} . The reaction equilibrium of fructose to HMF conversion can be reached within a few minutes at 140°C . Benefited from the surface acidity and microwave heating ability, the energy efficiency of the reaction by titanate nanotube ($5.6\text{ mmol (KJ L)}^{-1}$) is 9 times higher than commercial TiO_2 solid acid ($0.6\text{ mmol (KJ L)}^{-1}$). The interlayer polarization is revealed as the major reason for the enhanced microwave response of titanate catalyst and energy efficiency of the reactions.

1. Introduction

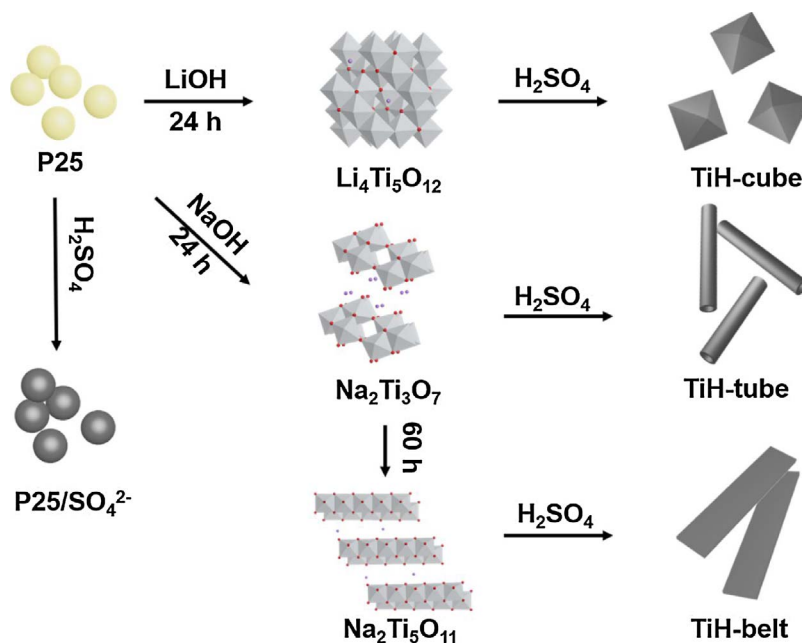
Exploration of sustainable energy is one of the most pursued research areas in this century to address the challenge of fossil fuel depletion [1–3]. Among the various sustainable energy strategies such as solar, wind, geothermal etc., biomass technology has its unique position among the list of sustainable energies since versatile chemical products can be produced rather than energy itself only [4–6]. The economic production of platform chemicals, such as 5-hydroxymethylfurfural (HMF), is well recognized as the key step in biomass conversion [7–10]. Therefore, the synthesis of HMF from carbohydrates (e.g. cellulose, saccharide) has become one of the most studied reactions during past decade [11,12]. HMF has been studied as starting material to produce biofuel products (e.g. 2,5-dimethylfuran and 5-ethoxymethylfurfural) and bioplastic monomers (e.g. 2,5-diformylfuran and 2,5-furandicarboxylic acid) [13–15].

Traditionally, long time reaction (1–6 h) at elevated temperature

(150 – 200°C) is often required to synthesize HMF [16–18]. Catalysts such as SnO_2 [19], ZrO_2 [20], TiO_2 [21], and zeolite [11], have been excavated to boost the dehydration rate and HMF yield. Microwave has been demonstrated effective energy input to expedite reaction rate, shorter reaction time and promote reaction efficiency [20,22–24]. For example, Wu et al. developed HNb_3O_8 as heterogeneous catalyst and reached HMF yield of up to 56% after 18 min of microwave treatment [22]. Compared to traditional heating, microwave heating shortened the reaction time, improved the HMF yield and more importantly avoided the massive formation of coke [22]. A well-known fact is that heterogeneous reactions occur at catalyst surface [25,26]. Heat needs to be transferred from heat source to catalyst surface in convective heating mode and only the part of heat reaches to catalyst surface can be utilized for reactions. That is said, a great amount of heat is not utilized for reaction, which is not necessary but unavoidable with convective heating. Microwave has been traditionally used as a heating method with rapid heating rate and uniform distribution of heat [27,28].

* Corresponding author.

E-mail address: jhzhu.yzu@gmail.com (J. Zhu).



Scheme 1. Synthetic route of three nano-titanates with different morphologies.

However, the selective heating on specific components in a reaction and saving reaction energy have not been explored yet. It is preferred to allocate all the heat energy at catalyst surface to maximize the usage of heat and boost energy efficiency of reactions. Realizing the fact that most of existing heterogeneous catalysts (e.g. TiO_2 , Niobic acid and Amberlyst-15) are microwave-transparent [29]. That is said, the catalyst itself does not absorb microwave and it does not contribute to the heating of the reaction system. The heat generated in the reaction is mainly contributed by polar solvent such as water [30,31]. Localized heat generation by catalyst itself could be more advantageous in terms of the heat utilization. Recently, our group developed core/shell structured microwave responsive catalysts with carbon nanotube core and TiO_2 shell [30]. With such structure, the heat generated at the core area by microwave radiation can be translated to the shell catalyst directly. Such localized heating maximized heat utilization in the reaction and uplifted energy efficiency of reaction by up to six times compared to pure TiO_2 .

Enabling microwave absorption of microwave-transparent material can be achieved by surface modification and crystal defect engineering [32–34]. For instance, Xia et al. found that hydrogenated TiO_2 nanocrystals can respond to electromagnetic wave at 2–18 GHz due to the formation of an amorphous TiO_2 layer on the surface after surface hydrogenation [34]. The interfacial polarization is proposed as the main reason for the induced microwave responsive behaviour, where the crystal defects play an important role at interface that triggers microwave absorption at the grain boundary.

TiO_2 nanomaterials (e.g. nanotube, nanobelt, nanosheet) synthesized from the layered titanates have been widely used as photo-catalyst [35], catalysis support [18,36], sensing material [37], and electrode for lithium battery [38]. The controllable shape, large surface-to-volume ratio and high sedimentation rate made them suitable catalyst for heterogeneous reactions [39–41]. During synthesis, the intermediates (protonated titanates, $\text{H}_2\text{Ti}_n\text{O}_{2n+1}$, $n = 3, 5$) are often overlooked due to their low-crystallinity. However, these intermediates show open monoclinic lattice structure with parallel corrugated layers of TiO_6 octahedra [40]. Such unique crystal structure allows infiltration of sulfate ions into titanate layers and then form polar Ti-O-SO_4^{2-} acid sites. Meanwhile, the crystal phase, morphology and phase composition of TiO_2 can be easily controlled through tuning synthetic conditions.

In this study, sulfate titanates were synthesized and used as microwave responsive catalysts for fructose conversion reactions. By

controlling the hydrothermal conditions, nanotube, nanotube and nanobelt shapes of titanate were synthesized. The ion-exchanged titanates were then directly heated to form *in-situ* Ti-O-SO_4^{2-} acid sites between the crystal layers of titanate. Taking advantage of the open crystal structure, more acid sites can be formed than that of commercial or other forms of TiO_2 . The effect of surface polarization on the microwave absorption of titanates was studied. The catalytic activity and energy efficiency of titanate catalysts were studied in fructose to HMF conversion reactions at different power levels. Combined with the structural and physicochemical features of nano-titanates, the mechanism of microwave absorption and the catalytic properties were proposed and systematically investigated.

2. Experimental

2.1. Materials

Lithium hydroxide (LiOH 98%), Sulfuric acid (H_2SO_4 95–98%), titania (TiO_2 nanopowder, > 99.5%), D-(–)-fructose ($\text{C}_6\text{H}_{12}\text{O}_6$ ≥ 99%), were purchased from Sigma-Aldrich. Sodium hydroxide (NaOH , 99%) was purchased from VWR. Ethanol (200 proof) was purchased from Decon Laboratories, Inc. All reagents were used as received without further purification. Deionized water was purified using a Milli-Q Direct 8 Ultrapure water system (Millipore, Billerica, MA) with a minimum resistivity of 18.2 MΩ cm.

2.2. Preparation of titanates

Titanates with three different nano-structures were prepared using the hydrothermal method, details refer to **Scheme 1**. Specifically, commercial P25 powder (1.0 g) was mixed with 20 mL of LiOH (10 M) or 20 mL of NaOH (10 M) aqueous solutions. The mixture was stirred thoroughly for 2 h and then placed into a Teflon-lined stainless steel autoclave. The autoclave was heated and kept at 150 °C for 24 h and then cooled down to room temperature. During the hydrothermal process, strong alkali broke the Ti-O bond in TiO_2 and formed new titanate structures. Three different forms of titanate crystal structures could be formed, $\text{Li}_4\text{Ti}_5\text{O}_{12}$, $\text{Na}_2\text{Ti}_3\text{O}_7$ and $\text{Na}_2\text{Ti}_5\text{O}_{11}$, depending on the alkali species and reaction time. The mixture was filtered to remove the excess alkali solution. The solid was washed by 500 mL H_2SO_4 solution (0.1 M) and freeze-dried. The samples were then heated at 380 °C for

3 h to form Ti-O-SO_4^{2-} structure. In this work, titanates prepared with LiOH and NaOH form nanocube and nanotube structures, and they were named TiH-NC and TiH-NT , respectively. By extending the reaction time from 24 to 60 h (other experimental procedure is the same as TiH-NT), nanobelts structure could be obtained and the sample is named TiH-NB . A control sample is also prepared with commercial P25. Specifically, P25 powder was firstly soaked with 0.1 M H_2SO_4 for 3 h, dried at 80 °C for 4 h, and then heated at 380 °C for 3 h in the air. Sample is named P25/SO_4^{2-} .

2.3. Characterizations

Material morphology was characterized by scanning electron microscopy (SEM, JEOL-7401) and transmission electron microscopy (FEI Scanning TEM). The powder X-ray diffraction analysis was carried out with a Bruker AXS D8 Discover diffractometer with GADDS (General Area Detector Diffraction System) operating with a Cu-K α radiation source filtered with a graphite monochromator ($\lambda = 1.541 \text{ \AA}$). The high resolution TEM (HRTEM, FEI Tecnai G2 F20 ST TEM/STEM & EDAX energy dispersive x-ray spectrometer) was adopted for further characterizing the crystal lattice. Raman spectra were obtained using a Horiba HR 800 spectrometer, equipped with a CCD camera detector. Brunauer–Emmett–Teller (BET) surface area analysis was measured using a TriStar II 3020 surface analyser (Micromeritics Instrument Corp., USA) by N_2 adsorption–desorption isotherms at 77 K. The pore size distribution was calculated by the Barrett–Joyner–Halenda (BJH) method from the adsorption branch. Energy dispersive x-ray spectrometer (EDX) was used to quantify the composition of surface elements.

2.4. Catalytic reaction under microwave irradiation

Dehydration reaction of fructose to HMF conversion was carried out in a quartz tube (10 mL, ID = 12 mm) under microwave irradiation. Typically, 0.55 mmol fructose and 50 mg catalyst were added into 4.0 mL water and then sonicated for 5 min. A small stirrer bar was used for mixing during microwave reaction. The loaded tube was then placed into the microwave reactor (Discover SP, CEM) and been exposed to microwave power (11–19 W) for a given time. After reaction, the resulting solution was cooled down and filtered by a syringe filter (VWR, 0.22 mm PTFE). Two reaction modes were adopted in this work to test catalyst performance, i.e. constant temperature and constant power modes. Constant temperature method was used to study the intrinsic catalytic activity, where the temperature was set at 130–150 °C and maximum pressure was controlled under 300 psi. The constant power method was used to study the microwave heating performance. The input power of microwave was adjusted between 11 and 19 W and maximum pressure was controlled under 300 psi. The filtrate was analyzed by both UV-vis spectrophotometry and HPLC equipped with RI detector and HPX-87 column with 0.17 mL/min of distilled water at 55 °C. The fructose conversion and HMF yield can be calculated by Eqs. (1) and (2):

$$\text{Fructose conversion}(\%) = \frac{\text{Fructose consumed(mol)}}{\text{Initial fructose(mol)}} \times 100 \quad (1)$$

$$\text{HMF yield}(\%) = \frac{\text{HMF produced(mol)}}{\text{Initial fructose(mol)}} \times 100 \quad (2)$$

3. Results and discussion

3.1. Microstructure

The XRD patterns of three titanates and P25/SO_4^{2-} are shown in Fig. 1(a1–a4). Diffraction patterns of P25/SO_4^{2-} show mixed crystal structures of anatase (JCPDS #02-0387) and rutile (JCPDS #04-0551), Fig. 1(a1). The sharp and intense peaks of P25/SO_4^{2-} indicate that the

crystal structures of P25 are well remained after doping surface sulfate groups. Three synthesized titanates show weak and broad diffraction peaks, indicating their low crystallinity feature. As showed in Fig. 1(a2), the peaks at 25.3, 36.9, 37.9, 48.1, 53.8, 55.3 and 64.2° are indexed to anatase phase and other peaks at 12.9, 29.3, 30.5 and 45.3° are the signatures of $\text{H}_2\text{Ti}_5\text{O}_{11}\cdot3\text{H}_2\text{O}$ (JCPDS #44-0130). $\text{H}_2\text{Ti}_5\text{O}_{11}\cdot3\text{H}_2\text{O}$ is derived from $\text{Li}_4\text{Ti}_5\text{O}_{11}$ after the ion-exchange process. The diffraction peaks of TiH-NT , Fig. 1(a3), revealed a mixed crystal structures of anatase and $\text{H}_2\text{Ti}_3\text{O}_7$ (JCPDS #47-0567). It is worth mentioning that both $\text{H}_2\text{Ti}_5\text{O}_{11}\cdot3\text{H}_2\text{O}$ and $\text{H}_2\text{Ti}_3\text{O}_7$ are intermediates with low-crystallinity since the layer crystal structure was collapsed during the ion-exchange step. In addition, the following calcination at relative low temperature of 380 °C is insufficient to reorganize the structure into well-patterned crystal phase. The diffraction pattern of TiH-NB is indexed to a mixed crystal structure of $\text{TiO}_2(\text{B})$ (JCPDS #35-0088) and $\text{H}_2\text{Ti}_5\text{O}_{11}\cdot3\text{H}_2\text{O}$, Fig. 1(a4). The XRD results reveal that $\text{Na}_2\text{Ti}_3\text{O}_7$ transforms to $\text{Na}_2\text{Ti}_5\text{O}_{11}$ by extending the hydrothermal reaction time from 24 to 60 h. The layers of $[\text{Ti}_3\text{O}_7]^{2-}$ are rearranged to $[\text{Ti}_5\text{O}_{11}]^{2-}$ with better stability [42] and part of $\text{H}_2\text{Ti}_5\text{O}_{11}\cdot3\text{H}_2\text{O}$ is dehydrated to form $\text{TiO}_2(\text{B})$ during calcination.

Raman spectroscopy was carried out to confirm the presence of mixed crystal structures of P25/SO_4^{2-} and three titanates, Fig. 1(b1–b4). Overall, peak intensity of synthesized titanates is relatively weaker than that of P25/SO_4^{2-} , indicating their loosely packed crystal structure. This phenomenon is consistent with the XRD results where all the titanates show broader crystal peaks than P25/SO_4^{2-} . P25/SO_4^{2-} is composed of anatase and rutile structures as evidenced by the five active modes of anatase (147, 198, 398, 515 and 640 cm^{-1}) and four active modes of rutile (144, 448, 612, and 827 cm^{-1}), Fig. 1(b1). Besides the anatase phase, six additional Raman bands at 128, 194, 270, 449, 629 and 908 cm^{-1} are observed in TiH-NC and TiH-NT (Fig. 1b2 and b3), which can be assigned to the stretching vibration of Ti–O bond and Ti–O–Ti framework of hydrated titanate [43–45]. The intensity of anatase bands in TiH-NC are stronger than that of TiH-NT , which indicates a larger fraction of anatase phase. A new $\text{TiO}_2(\text{B})$ phase was found in TiH-NB with signature vibration modes at 145, 237, 293, 359, 407, 427 and 653 cm^{-1} [46,47]. The Raman results clearly reveal the mixed crystal feature of TiO_2 and titanates, which are highly consistent with the XRD results.

TEM was performed to characterize the sample morphology of P25/SO_4^{2-} and three titanates. Fig. 2(a) show the image of the P25/SO_4^{2-} nanoparticles. These nanoparticles are mostly aggregated with single particle size of approximately 22.6 nm. Fig. 2(b) shows the octahedral-shaped titanate when 10 M LiOH was employed during the reaction. Each side of TiH-NC is approximately equal and the average length is $31.4 \pm 7.1 \text{ nm}$. Such octahedral-shaped morphology is derived from $\text{Li}_4\text{Ti}_5\text{O}_{12}$ crystal structure, which belongs to the cubic system with space group $\text{Fd}3\text{m}$ [48]. Fig. 2(c) showed the nanotube morphology with about 1 nm shell thickness. The statistical histogram of TiH-NT showed its outer diameter of $8.9 \pm 1.2 \text{ nm}$ within the range of 5–50 nm. The length of these nanotubes was ranged from 42 to 250 nm. Scrolling the exfoliated $\text{H}_2\text{Ti}_3\text{O}_7$ nanosheet into nanotube structure is well accepted explanation for the structural transformation, while the mechanism is still in debate [49]. By simply increasing the hydrothermal reaction time from 24 to 60 h, a larger size of belt-shaped titanate can be obtained, Fig. 2(d). The average width of TiH-NB is $51.4 \pm 20.5 \text{ nm}$ and the maximum length reaches up to 10 μm . Uniformly distributed nanopores of $\sim 5 \text{ nm}$ is also observed on the belt, inset of Fig. 2(d). These pores are formed during the assembling process of nanocrystals, as evidenced by the SEM results in Fig. S1.

The crystal structure reorganization during hydrothermal reaction not only affects the final morphology of the products, but also the surface area and pore structure. Fig. 3 showed the nitrogen adsorption–desorption isotherms for the samples at 77 K. All the four samples exhibited type IV isotherm curves with H_4 hysteresis loop [50]. The dominating adsorption of TiH-NT was occurred at high relative pressure (p/p_0

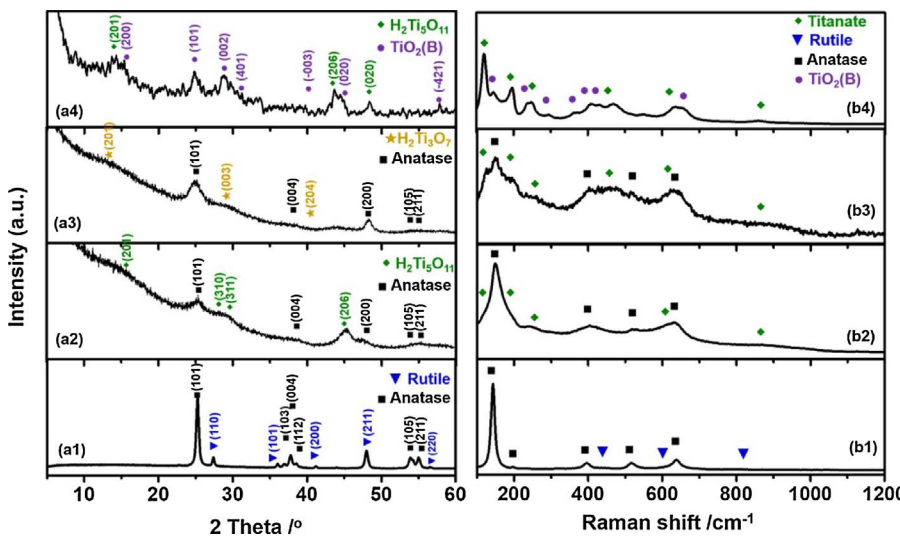


Fig. 1. XRD pattern and Raman spectrum of (a1, b1) P25/ SO_4^{2-} , (a2, b2) TiH-NC, (a3, b3) TiH-NT and (a4, b4) TiH-NB.

$p_0 > 0.8$), indicating its open porous structure [51] that is consistent with the TEM observation. As seen from the pore size distribution curve (inset of Fig. 3), TiH-NT shows a peak at ~ 4.5 nm corresponding to the inner diameter of TiH-NT. The BET surface area varies among the samples, i.e. P25/ SO_4^{2-} ($50 \text{ m}^2 \text{ g}^{-1}$), TiH-NC ($168 \text{ m}^2 \text{ g}^{-1}$), TiH-NT ($266 \text{ m}^2 \text{ g}^{-1}$), and TiH-NB ($54 \text{ m}^2 \text{ g}^{-1}$), respectively. The relatively larger surface area of TiH-NC compared to P25/ SO_4^{2-} and TiH-NB is attributed to its inner porous structure as evidenced by HRTEM in Fig. S2. Majority of the pore volume is located at ≤ 2 nm region, indicating the dominance of micropores in the materials.

The formation of Ti-O-SO_4^{2-} acidic site can be achieved by reaction at 380°C . The quantification of acid sites is critical since it directly influences the catalytic property [30]. In this work, EDX was conducted to quantify the acid sites on catalyst surface, Fig. 4(a–d). The quantity of sulfur element represents the quantity of SO_4^{2-} groups on the surface. The fraction of sulfur element in P25/ SO_4^{2-} , TiH-NC, TiH-NT, and TiH-NB was measured as 1.05, 1.98, 4.19 and 3.41 wt%, respectively. Providing the structural information in Table 1, it appeared that surface area was not the sole factor determining the quantity of SO_4^{2-} . For example, the surface area of TiH-NB and P25 is about the same, but the

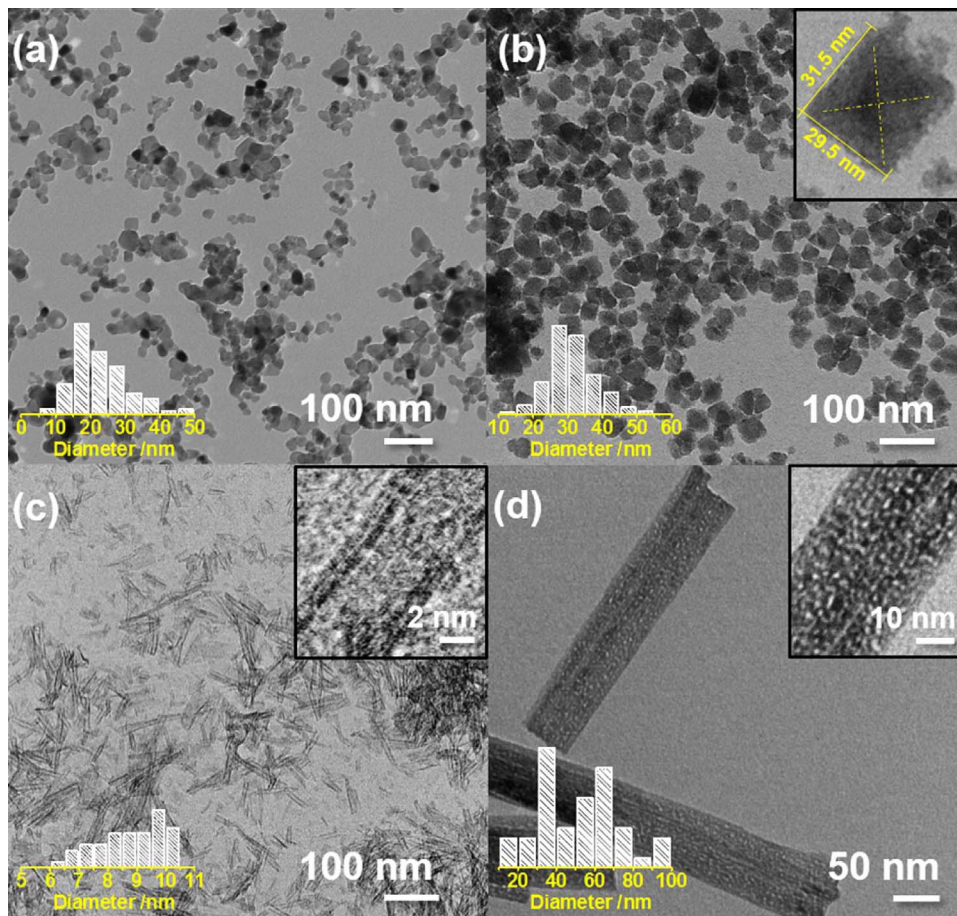


Fig. 2. TEM images of (a) P25/ SO_4^{2-} , (b) TiH-NC, (c) TiH-NT, and (d) TiH-NB and their corresponding size distribution (left bottom inset).

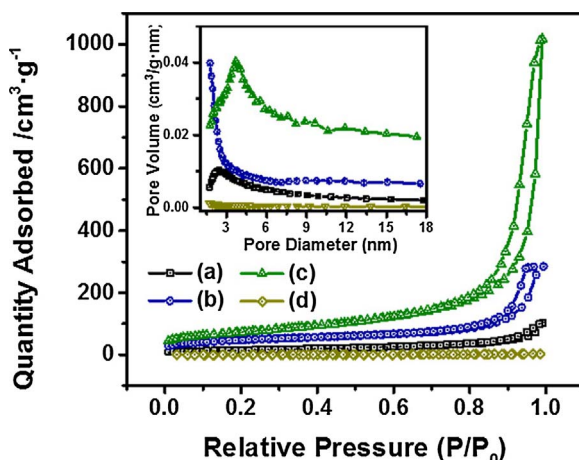


Fig. 3. Nitrogen adsorption-desorption isothermal of (a) P25/SO₄²⁻, (b) TiH-NC, (c) TiH-NT, and (d) TiH-NB. The inset shows the pore size distribution using BJH method.

sulfur content in TiH-NB is about three times of P25. It is speculated that the crystal form may also affect the acid site formation. The higher sulfur loading in titanates than P25 can be attributed to their open crystal structure, where SO₄²⁻ ions could permeate into the interlayer space of titanate crystal structures, Fig. 4(e). The highest sulfur content in TiH-NT reveals that H₂Ti₃O₇ intermediate has larger open channels than H₂Ti₅O₁₁ (intermediate of TiH-NB and TiH-NT), which promotes the acid site formation. In a word, the crystal structure of titanate intermediate has great influence on the formation of Ti-O-SO₄²⁻ acidic sites.

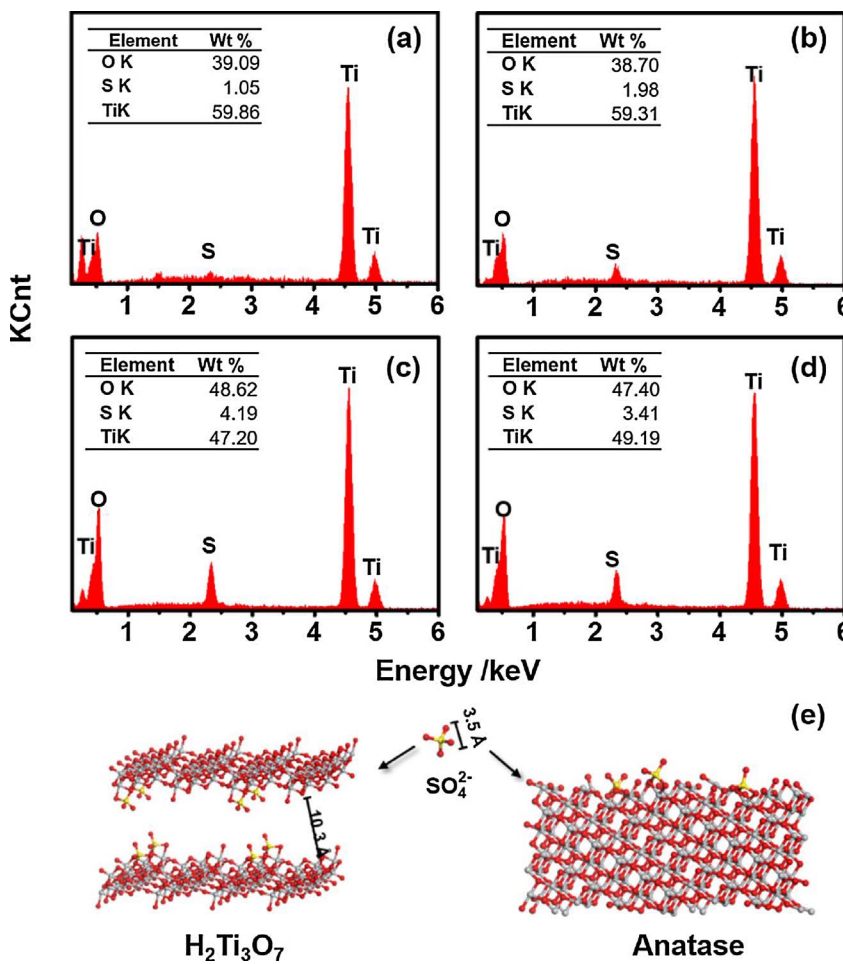


Fig. 4. EDX spectrum of (a) P25/SO₄²⁻, (b) TiH-NC, (c) TiH-NT, and (d) TiH-NB and scheme of sulphate modification on H₂Ti₃O₇ and anatase.

To further investigate the acid strength of the prepared catalysts, temperature-programmed desorption of NH₃ was performed. The amount of desorbed NH₃ allows a quantitative evaluation of the number of active sites, whereas the desorption temperature is an indicator of the acid strength. As seen in Fig. 5, all samples show three desorption peaks at < 200, 200–400, and 400–600 °C regions, which correspond to weak, medium-strong and strong acid sites, respectively [52,53]. The largest desorption peak appeared at the highest temperature region, indicating the dominance of strong acid sites in all the four materials. The desorption temperature of P25/SO₄²⁻ is relatively lower than that of TiH-NC, TiH-NT, and TiH-NB. Moreover, the amount of desorbed NH₃ is highly consistent with the variation of sulfur element (Fig. 4) in the four materials: P25/SO₄²⁻ < TiH-NC < TiH-NT < TiH-NB.

3.2. Intrinsic activity study

To screen the catalytic activity, isothermal reaction of fructose-to-HMF conversion was carried out. Fig. 6(a) shows the influence of reaction time on HMF yield at 140 °C. In the first 2 min, HMF yield was calculated to be 1.9, 5.0, 35.9, and 13.1 mol% with P25/SO₄²⁻, TiH-NC, TiH-NT and TiH-NB, respectively. TiH-NT exhibited significantly higher HMF conversion rate than the other catalysts. The HMF yield per minute by TiH-NT was significantly higher than other reported heterogeneous catalysts such as HNbO₃ [22], ZrPO [20], and NbPO [20] or even homogeneous catalysts of MgCl₂ [54] and HCl [55], Fig. 6(b). After 5 min, the fructose conversion reached to 75.9% together with the formation of side products, which was expected in aqueous systems because fructose dehydration is generally non-selective [56]. According to previous kinetic study, the dehydration of fructose can be considered

Table 1
Summary of morphology, porous structure and crystalline forms.

	Morphology	Structure	Crystalline			
P25	Shape	$r_{l/d}$ ^a	SA ($m^2 g^{-1}$)	V_p ($cm^3 g^{-1}$)	d_p (nm)	Crystal form
TiH-NC	Nanoparticle	1.2	50	0.1	5.1	Anatase + Rutile
TiH-NT	Nanocube	1	168	0.2	5.4	Anatase + $H_2Ti_3O_{11}$
TiH-NB	Nanotube	10.3	266	0.4	6.4	Anatase + $H_2Ti_3O_7$
	Nanobelt	> 50	54	0.1	9.6	$TiO_2(B) + H_2Ti_5O_{11}$

^a aspect ratio.

^b TiO_2 crystal size.

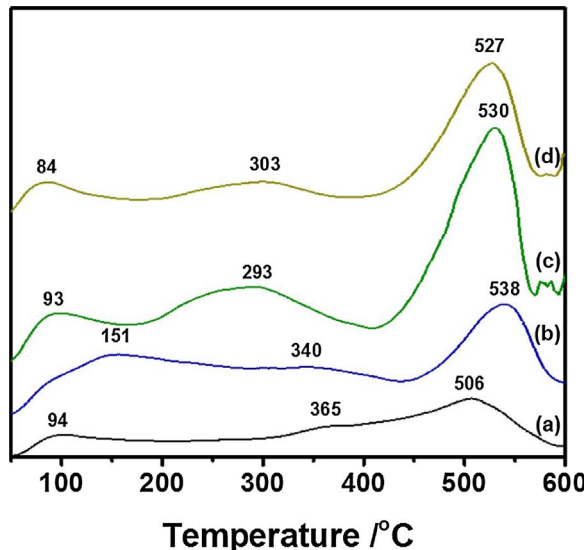


Fig. 5. NH_3 -TPD patterns of (a) $P25/SO_4^{2-}$, (b) TiH-NC, (c) TiH-NT and (d) TiH-NB.

as a pseudo-first order reaction. This assumption is valid only when HMF is stable and no side products are formed. With this assumption, rate of fructose ($r_{fructose}$) conversion can be expressed in Eq. (3):

$$r_{fructose} = \frac{d(\ln(C_t/C_0))}{dt} = -k \quad (3)$$

where C_0 is initial fructose concentration, C_t is fructose concentration at time t , k is the rate constant of fructose dehydration at a certain temperature. After data fitting, the $\ln(C_t/C_0)$ versus t showed a good linear relation (Fig. 6c) that well supported the hypothesis of pseudo-first order reaction. The rate constant k was calculated to be 0.02, 0.07, 0.31 and 0.17 min^{-1} for $P25/SO_4^{2-}$, TiH-NC, TiH-NT and TiH-NB. TiH-NT acquired the largest reaction rate, which was about 15 times higher than $P25/SO_4^{2-}$. The variation of rate constant k was in good agreement with the quantity of sulfate groups at catalyst surface, *i.e.* reaction rate increased with increasing the amount of sulfate group. Therefore, the catalyst activity is highly dependent on the crystal structure and surface area of the titanates. Titanates of different morphologies in this work offer a series combination of crystal structure and surface area that results in an optimized catalytic property in TiH-NT.

To have a better understanding of the surface reaction, activation energy (E_a) of the four catalysts was evaluated. E_a is an empirical parameter that represents the energy required to overcome the energy barrier for specific chemical reactions [57,58]. To acquire E_a for each catalyst, the reactions were performed at three temperatures of 130, 140 and 150 °C. The results of HMF yield and reaction rate at each temperature were summarized in Fig. S3. In general, the reaction rate increased with increasing temperature from 130 to 150 °C. The E_a can be assessed from the Arrhenius Eq. (4):

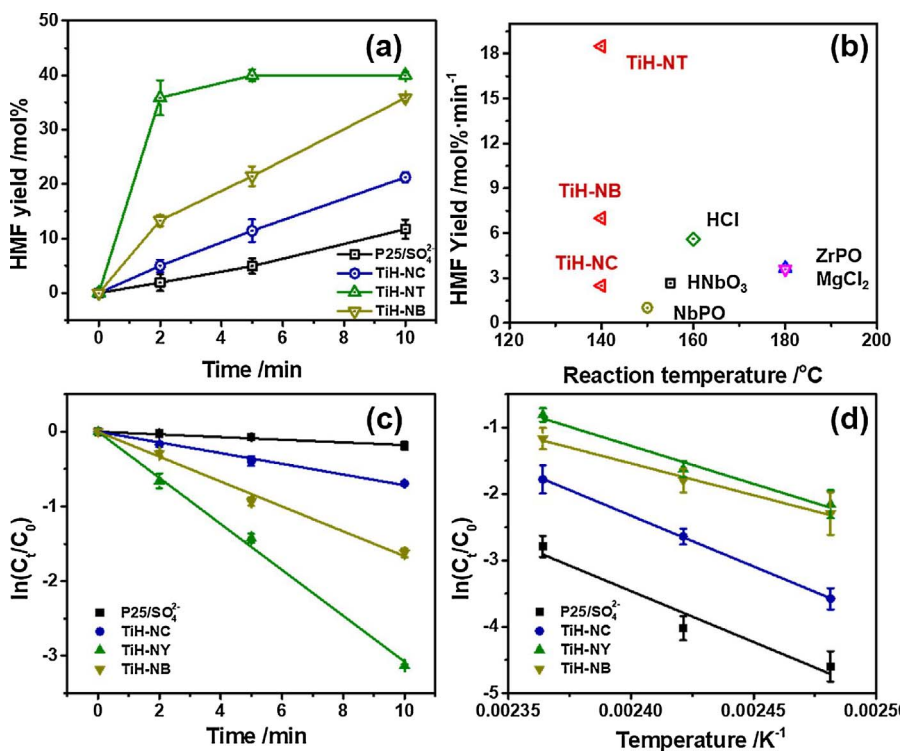


Fig. 6. (a) HMF yield by four catalysts, (b) HMF yield comparison with published results, (c) Plots of $\ln(C_t/C_0)$ versus reaction time of fructose dehydration and the inset indicates the relation of sulfur amount with reaction rate constant k , (d) Arrhenius plots of four catalysts. Reaction condition: [fructose] = 0.55 mmol, [catalysts] = 12.5 mg/mL, temperature = 140 °C.

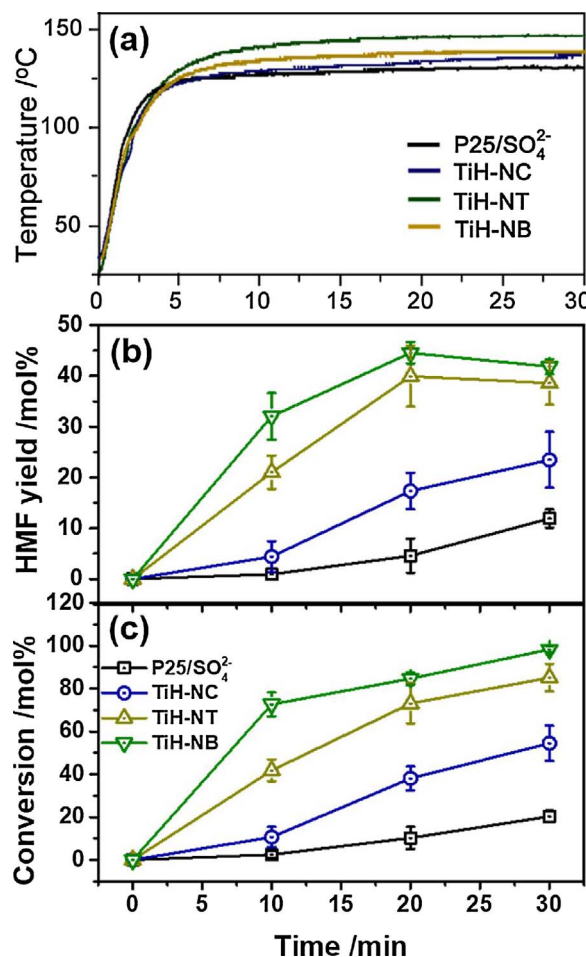


Fig. 7. (a) System temperature profile, (b) HMF yield and (c) fructose conversion as a function of reaction time by using P25/SO₄²⁻, TiH-NC, TiH-NT, and TiH-NB catalysts. Reaction condition: [fructose] = 0.55 mmol, [catalysts] = 12.5 mg/mL, input power = 15 W.

$$k = A \times \exp\left(-E_a/RT\right) \quad (4)$$

where A is Arrhenius factor, k is the rate constant of the reaction at temperature T . E_a can be calculated from the slope of $\ln k$ versus $1/T$ linear curve Fig. 6(d). The E_a value was calculated as 127.6, 127.3, 95.6 and 91.1 kJ/mol for P25/SO₄²⁻, TiH-NC, TiH-NT and TiH-NB, respectively. These results suggested that less energy was required to proceed the reaction on TiH-NT and TiH-NB than that of P25/SO₄²⁻ and TiH-NC. In other words, more energy can be utilized for reaction by using TiH-NT and TiH-NB catalysts due to the presence of more active sites and better microwave absorption property.

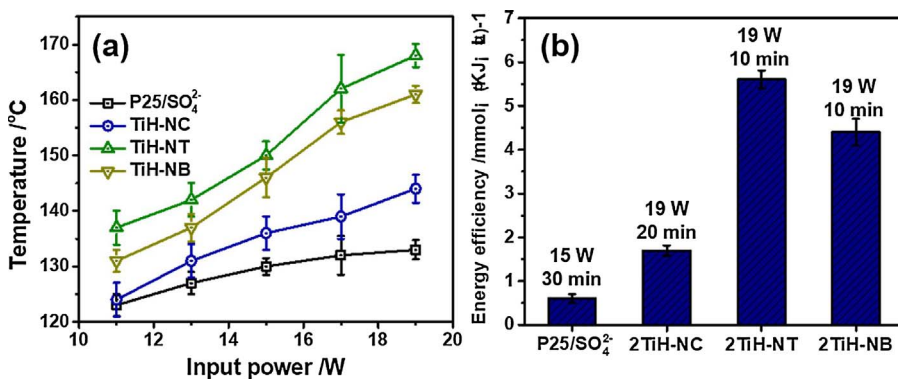


Fig. 8. (a) Equilibrium temperature as a function of input power and (b) energy efficiency by using P25/SO₄²⁻, TiH-NC, TiH-NT, and TiH-NB catalysts. Reaction condition: [fructose] = 0.55 mmol, [catalysts] = 12.5 mg/mL.

3.3. Microwave heating study

The microwave absorption property of four catalysts was investigated by fixing microwave input power at 15 W. As seen in Fig. 7(a), the temperature of the reaction solution ramped up rapidly in the first a few minutes and then gradually stabilized afterwards. The equilibrium temperature (after 15 min) for the four catalysts was in the range of 130–150 °C. TiH-NT acquired the highest temperature of 150 °C and the lowest of 130 °C was observed in P25/SO₄²⁻. The highest equilibrium temperature observed in TiH-NT system was attributed to the better capability of TiH-NT in microwave absorption and heat generation. Higher reaction temperature accelerated the reaction rate and shifted reaction equilibrium to product side since fructose conversion to HMF was a well-known endothermic process [59]. By using TiH-NT catalyst, the HMF yield and fructose conversion reached to 45 and 78 mol% in 20 min, Fig. 7(b and c).

The synthesized titanates show obvious advantage compared to P25 in terms of the better heating capability with increasing microwave power. Fig. 8(a) showed the equilibrium temperature of reaction solution as a function of microwave input power. Apparently, larger power input led to higher temperature ramping rate (Fig. S4-7) and system equilibrium temperature. Setting input power at 11 W, the equilibrium temperature of P25/SO₄²⁻, TiH-NC, TiH-NT, and TiH-NB was 123, 123, 137, and 131 °C, which increased by 10, 20, 31 and 30 °C respectively after adjusting power from 11 to 19 W.

In our previous work, energy efficiency was introduced to evaluate catalyst performance in microwave-assisted HMF synthesis. Energy efficiency η is defined in Eq. (6) that describes the amount of HMF produced by consuming per unit of work.

$$\text{Energy efficiency } \eta = \frac{[\text{HMF}]}{P \cdot t \cdot V} \quad (6)$$

where P is input power of microwave, t is elapsed time and V is volume of reaction solution. The energy efficiency of four catalysts was calculated at different power levels with different reaction times. Specific catalytic performance results were summarized in Fig. S4-7. The highest energy efficiency reached in each catalyst was 0.6, 1.7, 5.6 and 4.4 mmol (KJ L)⁻¹ for P25/SO₄²⁻, TiH-NC, TiH-NT and TiH-NB, respectively. Benefited from the stronger acidity and better microwave absorption property, the energy efficiency of TiH-NT was 9 times higher than commercial P25 solid acid in HMF production.

Microwave absorption of materials is often related to the dipole rotation of polar units or groups. The frequent alignment of polar groups with alternating electromagnetic field forces strong vibration of polar groups and friction with neighboring molecules. The frequent friction generates large amount of local heat surrounding those polar groups. From the structure point of view, polarization is related to crystal defects and material morphology. Crystal defects, such as dislocations or grain boundaries, electronic defects or phase boundaries, can lead to interfacial polarization. Charge transfer and accumulation at the interface induce significant dielectric loss. Besides, researchers

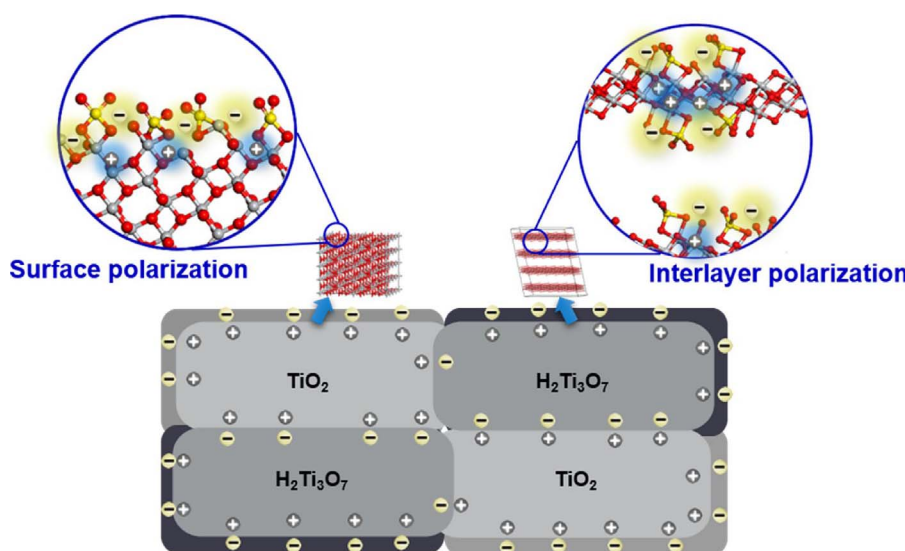


Fig. 9. Proposed mechanism of polarization on TiO_2 and $\text{H}_2\text{Ti}_3\text{O}_7$.

found that microwave absorption also depends on material morphology. For instance, Cao et al. found that cage like ZnO nanostructures showed relatively stronger microwave absorption in the X band, when compared with ZnO nanoparticles. Though different mechanisms have been proposed to explain the microwave absorption behavior of different materials, the main contribution of microwave absorption in titanate catalysts is surface polarization, as illustrated in Fig. 9. Specifically, sulfated TiO_2 forms Brønsted acid site on O^- and Lewis acid site on Ti^+ . These acid sites would accelerate charge transfer and form electrical dipole moment on the surface. As a result, such polarized surface becomes very active in electromagnetic field that helps to generate significant amount of heat. The surface sulfate group not only acts as catalytic active sites, but also the hot-spot for generating heat. All the generated heat can be in-situ utilized for reaction and thus better energy efficiency of the reaction could be achieved.

To verify the role of surface sulfate group in generating heat, a set of control experiments is performed to de-dope sulfate group by using 10 wt% ammonia solutions after the ion-exchange step. After calcination at 380 °C, the material morphology kept the same, yet the sulfur element disappeared, Fig. S8(a–c). By using de-doped catalysts in the same reaction system at 15 W power, a significant temperature drop of reaction solution was observed from each catalyst, Fig. 10. The equilibrium temperature of four reaction systems was about the same and slightly higher than a blank solution. Therefore, it is confirmed that surface polarization by sulfate group at catalyst surface is the major reason for their microwave response behavior. This result is also

consistent with our previous observation on the positive relation between microwave heating ability and sulfur content in catalysts. The better microwave heating capability of synthesized titanate catalysts than commercial P25 could be attributed to their open crystal structure as well. As illustrated in Fig. 9, sulfate ions could penetrate in the interlayer space of titanate and promote interlayer polarization. Not only the layer structure was beneficial to microwave absorption, the enlarged polarization area at interlayer space also further strengthened the capability of generating heat.

4. Conclusions

In summary, surface polarized titanates of different nanostructures, nanocube (TiH-NC), nanotube (TiH-NT) and nanobelt (TiH-NB), were successfully synthesized and used as microwave responsive catalysts for fructose dehydration reactions. TiH-NT exhibited the largest reaction rate constant of 0.31 min^{-1} and the corresponding HMF yield of 35.9 mol% in the first 2 min of reaction. Kinetic study showed lower activation energy of TiH-NT and TiH-NB than that of P25/ SO_4^{2-} and TiH-NC. Among the four catalysts, TiH-NT showed the best microwave absorption and heat generation properties. By using TiH-NT catalyst, the energy efficiency of HMF production reached to $5.6 \text{ mmol (kJ L)}^{-1}$, which was 9 times higher than commercial TiO_2 solid acid ($0.6 \text{ mmol (kJ L)}^{-1}$). In this work, the sulfate groups at catalyst surface not only serve as polarization center to generate heat under microwave, but also act as catalytic acid sites for the conversion reaction. The overwhelming advantage of such catalysts is that the heat generated can be directly used exactly where heat is needed for the reaction. Therefore, majority of the heat can be utilized in the reaction and thus improve the overall energy efficiency of the reaction.

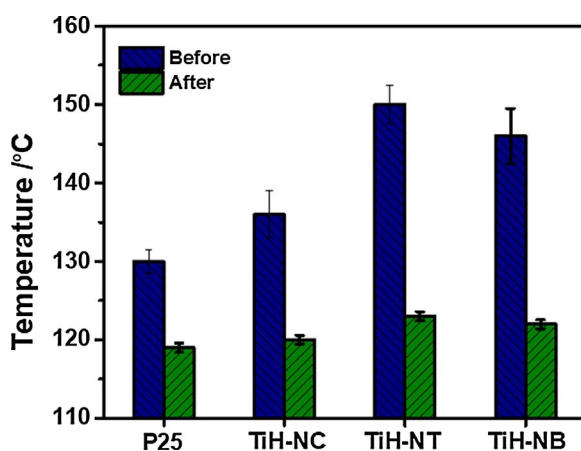


Fig. 10. The system temperature by using four de-doped materials.

Acknowledgements

The Acknowledgement is made to the Donors of the American Chemical Society Petroleum Research Fund (#55570-DNI10) and NSF (CBET-1603264). This work is also partially supported by Chinese MOST 973 project (2013CB733501), National Natural Science Foundation of China (21476106). The authors appreciate the instrument support from Prof. Lukwang Ju's group. HRTEM was performed at the Liquid Crystal Institute, Kent State University, supported by the Ohio Research Scholars Program Research Cluster on Surfaces in Advanced Materials. The authors appreciate the technical support with HRTEM from Min Gao.

Appendix A. Supplementary data

Supplementary data associated with this article can be found, in the online version, at <https://doi.org/10.1016/j.apcatb.2017.12.073>.

References

- [1] R. Tu, S. Chen, W. Cao, S. Zhang, L. Li, T. Ji, J. Zhu, J. Li, X. Lu, The effect of H₂O₂ desorption on achieving improved selectivity for direct synthesis of H₂O₂ over TiO₂(B)/anatase supported Pd catalyst, *Catal. Commun.* 89 (2017) 69–72.
- [2] T. Ji, L. Chen, M. Schmitz, F.S. Bao, J. Zhu, Hierarchical macrotube/mesopore carbon decorated with mono-dispersed Ag nanoparticles as a highly active catalyst, *Green Chem.* 17 (2015) 2515–2523.
- [3] J. Restrepo, R. Porcar, P. Lozano, M. Isabel Burguete, E. Garcia-Verdugo, S.V. Luis, Microwave-assisted selective oxidation of 1-Phenyl ethanol in water catalyzed by metal nanoparticles immobilized onto supported ionic liquid like phases, *ACS Catal.* 5 (2015) 4743–4750.
- [4] G. Kumar, S. Shobana, W.-H. Chen, Q.-V. Bach, S.-H. Kim, A. Atabani, J.-S. Chang, A review of thermochemical conversion of microalgal biomass for biofuels: chemistry and processes, *Green Chem.* 19 (2017) 44–67.
- [5] I. Delidovich, R. Palkovits, Catalytic isomerization of biomass-derived aldoses: a review, *ChemSusChem* 9 (2016) 547–561.
- [6] C. Yang, R. Li, C. Cui, S. Liu, Q. Qiu, Y. Ding, Y. Wu, B. Zhang, Catalytic hydro-processing of microalgae-derived biofuels: a review, *Green Chem.* 18 (2016) 3684–3699.
- [7] A. Dibenedetto, M. Aresta, L. di Bitonto, C. Pastore, Organic carbonates: efficient extraction solvents for the synthesis of HMF in aqueous media with cerium phosphates as catalysts, *ChemSusChem* 9 (2016) 118–125.
- [8] G. Tsilomeleakis, M.J. Orella, Z. Lin, Z. Cheng, W. Zheng, V. Nikolakis, D.G. Vlachos, Molecular structure, morphology and growth mechanisms and rates of 5-hydroxymethyl furfural (HMF) derived humins, *Green Chem.* 18 (2016) 1983–1993.
- [9] H.M. Mirzaei, B. Karimi, Sulphanilic acid as a recyclable bifunctional organocatalyst in the selective conversion of lignocellulosic biomass to 5-HMF, *Green Chem.* 18 (2016) 2282–2286.
- [10] C. Antonetti, M. Melloni, D. Licursi, S. Fulignati, E. Ribechini, S. Rivas, J.C. Parajó, F. Cavani, A.M.R. Galletti, Microwave-assisted dehydration of fructose and inulin to HMF catalyzed by niobium and zirconium phosphate catalysts, *Appl. Catal. B* 206 (2017) 364–377.
- [11] J.S. Kruger, V. Choudhary, V. Nikolakis, D.G. Vlachos, Elucidating the roles of zeolite H-BEA in aqueous-phase fructose dehydration and HMF rehydration, *ACS Catal.* 3 (2013) 1279–1291.
- [12] A. Osatiashvili, A.F. Lee, M. Granollers, D.R. Brown, L. Olivi, G. Morales, J.A. Melero, K. Wilson, Hydrothermally stable, conformal, sulfated zirconia mono layer catalysts for glucose conversion to 5-HMF, *ACS Catal.* 5 (2015) 4345–4352.
- [13] Z.H. Zhang, K.J. Deng, Recent advances in the catalytic synthesis of 2,5-Furandicarboxylic acid and its derivatives, *ACS Catal.* 5 (2015) 6529–6544.
- [14] B. Liu, Z.H. Zhang, One-pot conversion of carbohydrates into furan derivatives via furfural and 5-Hydroxymethylfurfural as intermediates, *Chemsuschem* 9 (2016) 2015–2036.
- [15] X. Kong, Y.F. Zhu, H.Y. Zheng, X.Q. Li, Y.L. Zhu, Y.W. Li, Ni nanoparticles inlaid nickel phyllosilicate as a metal-acid bifunctional catalyst for low-temperature hydrogenolysis reactions, *ACS Catal.* 5 (2015) 5914–5920.
- [16] R. Weingarten, J. Cho, R. Xing, W.C. Conner, G.W. Huber, Kinetics and reaction engineering of levulinic acid production from aqueous glucose solutions, *ChemSusChem* 5 (2012) 1280–1290.
- [17] M.I. Alam, S. De, B. Singh, B. Saha, M.M. Abu-Omar, Titanium hydrogenphosphate: an efficient dual acidic catalyst for 5-hydroxymethylfurfural (HMF) production, *Appl. Catal. A* 486 (2014) 42–48.
- [18] M. Yabushita, H. Kobayashi, K. Hara, A. Fukuoka, Quantitative evaluation of ball-milling effects on the hydrolysis of cellulose catalysed by activated carbon, *Catal. Sci. Technol.* 4 (2014) 2312–2317.
- [19] A. Dutta, D. Gupta, A.K. Patra, B. Saha, A. Bhaumik, Synthesis of 5-Hydroxymethylfurfural from carbohydrates using large-pore mesoporous tin phosphate, *Chemsuschem* 7 (2014) 925–933.
- [20] C. Antonetti, M. Melloni, D. Licursi, S. Fulignati, E. Ribechini, S. Rivas, J.C. Parajo, F. Cavani, A.M.R. Galletti, Microwave-assisted dehydration of fructose and inulin to HMF catalyzed by niobium and zirconium phosphate catalysts, *Appl. Catal. B* 206 (2017) 364–377.
- [21] L. Atanda, S. Mukundan, A. Shrotri, Q. Ma, J. Beltramini, Catalytic conversion of glucose to 5-Hydroxymethyl-furfural with a phosphated TiO₂ catalyst, *Chemcatchem* 7 (2015) 781–790.
- [22] Q.B. Wu, Y.N. Yan, Q. Zhang, J.H. Lu, Z.J. Yang, Y.H. Zhang, Y. Tang, Catalytic dehydration of carbohydrates on InSitu exfoliable layered niobic acid in an aqueous system under microwave irradiation, *Chemsuschem* 6 (2013) 820–825.
- [23] Y.X. Wang, C.M. Pedersen, T.S. Deng, Y. Qiao, X.L. Hou, Direct conversion of chitin biomass to 5-hydroxymethylfurfural in concentrated ZnCl₂ aqueous solution, *Bioresour. Technol.* 143 (2013) 384–390.
- [24] B. Saha, S. De, M.H. Fan, Zr(O)Cl₂ catalyst for selective conversion of biorenewable carbohydrates and biopolymers to biofuel precursor 5-hydroxymethylfurfural in aqueous medium, *Fuel* 111 (2013) 598–605.
- [25] R.M. Ziff, E. Gulari, Y. Barshad, Kinetic phase transitions in an irreversible surface-reaction model, *Phys. Rev. Lett.* 56 (1986) 2553.
- [26] Y.-C. Lin, G.W. Huber, The critical role of heterogeneous catalysis in lignocellulosic biomass conversion, *Energy Environ. Sci.* 2 (2009) 68–80.
- [27] A. Lew, P.O. Krutzik, M.E. Hart, A.R. Chamberlin, Increasing rates of reaction: microwave-assisted organic synthesis for combinatorial chemistry, *J. Comb. Chem.* 4 (2002) 95–105.
- [28] A. de la Hoz, A. Diaz-Ortiz, A. Moreno, Microwaves in organic synthesis. Thermal and non-thermal microwave effects, *Chem. Soc. Rev.* 34 (2005) 164–178.
- [29] M. Omri, G. Pourceau, M. Becuwe, A. Wadouachi, Improvement of gold-catalyzed oxidation of free carbohydrates to corresponding aldonates using microwaves, *ACS Sustain. Chem. Eng.* 4 (2016) 2432–2438.
- [30] T. Ji, R. Tu, L. Mu, X. Lu, J. Zhu, Enhancing energy efficiency in Saccharide–HMF conversion with core/shell structured microwave responsive catalysts, *ACS Sustain. Chem. Eng.* 5 (2017) 4352–4358.
- [31] A.K. Rathi, M.B. Gawande, R. Borbil, R.S. Varma, Microwave-assisted synthesis – catalytic applications in aqueous media, *Coord. Chem. Rev.* 291 (2015) 68–94.
- [32] J. Liu, J. Xu, R. Che, H. Chen, M. Liu, Z. Liu, Hierarchical Fe3O4@TiO2 yolk-Shell microspheres with enhanced microwave-absorption properties, *Chem. Eur. J.* 19 (2013) 6746–6752.
- [33] M. Zhou, X. Zhang, J. Wei, S. Zhao, L. Wang, B. Feng, Morphology-controlled synthesis and novel microwave absorption properties of hollow urchinlike α -MnO₂ nanostructures, *J. Phys. Chem. C* 115 (2010) 1398–1402.
- [34] T. Xia, C. Zhang, N.A. Oyler, X. Chen, Hydrogenated TiO₂ nanocrystals: a novel microwave absorbing material, *Adv. Mater.* 25 (2013) 6905–6910.
- [35] M. Andersson, L. Österlund, S. Ljungström, A. Palmqvist, Preparation of nanosize anatase and rutile TiO₂ by hydrothermal treatment of microemulsions and their activity for photocatalytic wet oxidation of phenol, *J. Phys. Chem. B* 106 (2002) 10674–10679.
- [36] W. Yuan, J. Li, L. Wang, P. Chen, A. Xie, Y. Shen, Nanocomposite of N-doped TiO₂ nanorods and graphene as an effective electrocatalyst for the oxygen reduction reaction, *ACS Appl. Mater. Interfaces* 6 (2014) 21978–21985.
- [37] S.J. Bao, C.M. Li, J.F. Zang, X.Q. Cui, Y. Qiao, J. Guo, New nanostructured TiO₂ for direct electrochemistry and glucose sensor applications, *Adv. Funct. Mater.* 18 (2008) 591–599.
- [38] L. Kavan, M. Kalbáč, M. Zukalová, I. Exnar, V. Lorenzen, R. Nesper, M. Graetzel, Lithium storage in nanostructured TiO₂ made by hydrothermal growth, *Chem. Mater.* 16 (2004) 477–485.
- [39] G. Tian, H. Fu, L. Jing, B. Xin, K. Pan, Preparation and characterization of stable biphase TiO₂ photocatalyst with high crystallinity, large surface area, and enhanced photoactivity, *J. Phys. Chem. C* 112 (2008) 3083–3089.
- [40] H.-H. Ou, S.-L. Lo, Review of titania nanotubes synthesized via the hydrothermal treatment, fabrication, modification, and application, *Sep. Purif. Technol.* 58 (2007) 179–191.
- [41] S.G. Kumar, L.G. Devi, Review on modified TiO₂ photocatalysis under UV/visible light: selected results and related mechanisms on interfacial charge carrier transfer dynamics, *J. Phys. Chem. A* 115 (2011) 13211–13241.
- [42] W. Li, Y. Bai, W. Zhuang, K.-Y. Chan, C. Liu, Z. Yang, X. Feng, X. Lu, Highly crystalline mesoporous TiO₂ (B) nanofibers, *J. Phys. Chem. C* 118 (2014) 3049–3055.
- [43] R. Ma, K. Fukuda, T. Sasaki, M. Osada, Y. Bando, Structural features of titanate Nanotubes/Nanobelts revealed by raman, X-ray absorption fine structure and electron diffraction characterizations, *J. Phys. Chem. B* 109 (2005) 6210–6214.
- [44] C. Guo, L. Xu, J. He, L. Hu, B. Wang, L. Da, Enhanced photocatalytic activity by Cu₂O nanoparticles integrated H₂Ti3O₇ nanotubes for removal of mercaptan, *Nano* (2017) 1750075.
- [45] H. Kim, F. Miyaji, T. Kokubo, T. Nakamura, Effect of heat treatment on apatite-forming ability of Ti metal induced by alkali treatment, *J. Mater. Sci. Mater. Med.* 8 (1997) 341–347.
- [46] A.G. Dylla, P. Xiao, G. Henkelman, K.J. Stevenson, Morphological dependence of lithium insertion in nanocrystalline TiO₂(B) nanoparticles and nanosheets, *J. Phys. Chem. Lett.* 3 (2012) 2015–2019.
- [47] G. Wang, Q. Wang, W. Lu, J. Li, Photoelectrochemical study on charge transfer properties of TiO₂-B nanowires with an application as humidity sensors, *J. Phys. Chem. B* 110 (2006) 22029–22034.
- [48] K. Teshima, H. Inagaki, S. Tanaka, K. Yubuta, M. Hozumi, K. Kohama, T. Shishido, S. Oishi, Growth of well-developed Li₄Ti₅O₁₂ crystals by the cooling of a sodium chloride flux, *Cryst. Growth Des.* 11 (2011) 4401–4405.
- [49] Y. Kobayashi, H. Hata, M. Salama, T.E. Mallouk, Scrolled sheet precursor route to niobium and tantalum oxide nanotubes, *Nano Lett.* 7 (2007) 2142–2145.
- [50] T. Ji, L. Chen, L. Mu, R. Yuan, M. Knoblauch, F.S. Bao, Y. Shi, H. Wang, J. Zhu, Green processing of plant biomass into mesoporous carbon as catalyst support, *Chem. Eng. J.* 295 (2016) 301–308.
- [51] T. Ji, L. Chen, L. Mu, R. Yuan, M. Knoblauch, F.S. Bao, J. Zhu, In-situ reduction of Ag nanoparticles on oxygenated mesoporous carbon fabric: exceptional catalyst for nitroaromatics reduction, *Appl. Catal. B* 182 (2016) 306–315.
- [52] M. Watanabe, Y. Aizawa, T. Iida, R. Nishimura, H. Inomata, Catalytic glucose and fructose conversions with TiO₂ and ZrO₂ in water at 473 K: relationship between reactivity and acid?base property determined by TPD measurement, *Appl. Catal. A* 295 (2005) 150–156.
- [53] F. Lónyi, J. Valyon, J. Engelhardt, F. Mizukami, Characterization and catalytic properties of sulfated ZrO₂?TiO₂ mixed oxides, *J. Catal.* 160 (1996) 279–289.
- [54] M. Francavilla, S. Intini, L. Luchetti, R. Luque, Tunable microwave-assisted aqueous conversion of seaweed-derived agarose for the selective production of 5-hydroxymethylfurfural/levulinic acid, *Green Chem.* 18 (2016) 5971–5977.

[55] T.S. Hansen, J.M. Woodley, A. Riisager, Efficient microwave-assisted synthesis of 5-hydroxymethylfurfural from concentrated aqueous fructose, *Carbohydr. Res.* 344 (2009) 2568–2572.

[56] M. Bicker, D. Kaiser, L. Ott, H. Vogel, Dehydration of d-fructose to hydroxymethylfurfural in sub- and supercritical fluids, *J. Supercrit. Fluids* 36 (2005) 118–126.

[57] B. Girisuta, L. Janssen, H. Heeres, A kinetic study on the decomposition of 5-hydroxymethylfurfural into levulinic acid, *Green Chem.* 8 (2006) 701–709.

[58] M. Liang, R.X. Su, W. Qi, Y.J. Yu, L.B. Wang, Synthesis of well-dispersed Ag nanoparticles on eggshell membrane for catalytic reduction of 4-nitrophenol, *J. Mater. Sci.* 49 (2014) 1639–1647.

[59] S. Caratzoulas, D.G. Vlachos, Converting fructose to 5-hydroxymethylfurfural: a quantum mechanics/molecular mechanics study of the mechanism and energetics, *Carbohydr. Res.* 346 (2011) 664–672.